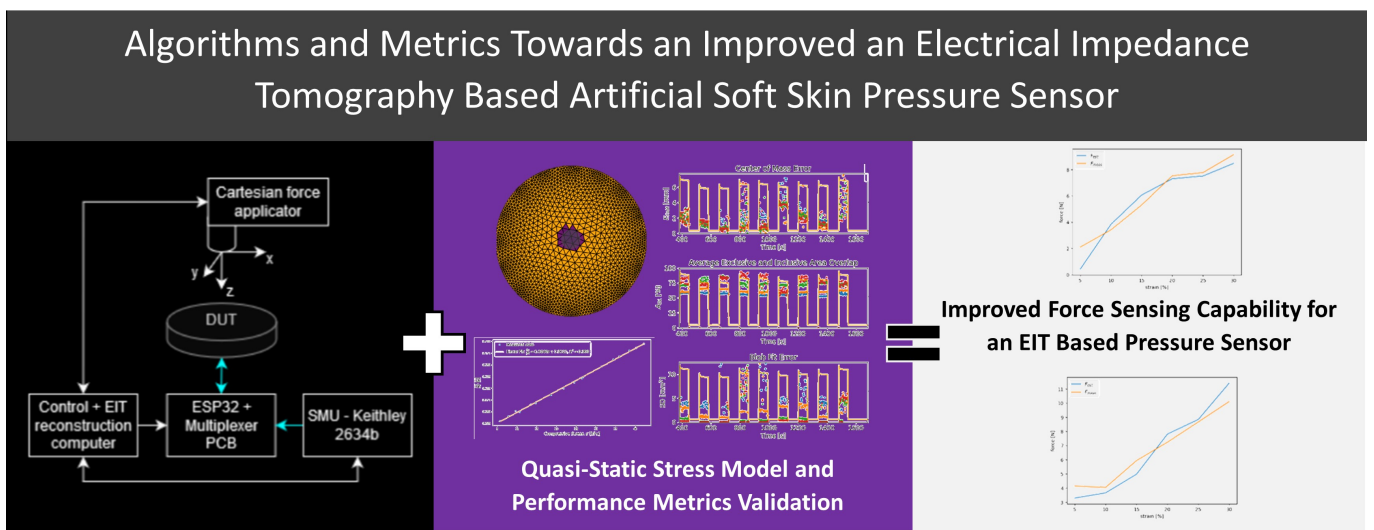


Graphical Abstract

Algorithms and Metrics Towards an Improved an Electrical Impedance Tomography Based Artificial Soft Skin Pressure Sensor

Richie Ellingham, Chris Pretty, Lui Holder-Pearson, Kean Aw, Tim Giffney



Highlights

Algorithms and Metrics Towards an Improved an Electrical Impedance Tomography Based Artificial Soft Skin Pressure Sensor

Richie Ellingham, Chris Pretty, Lui Holder-Pearson, Kean Aw, Tim Giffney

- Electrical impedance tomography is a valid method for detecting 2D transient resistive events in a piezoresistive soft pressure sensor platform.
- A quasi-static 1D stress to resistance model can be applied to a 2D surface to create a pressure map and generate pressure values.
- A collection of performance metrics have been deduced for further research and validation of a 2D EIT sensor. Useful for development with different materials in various applications.
- An inhomogeneous piezoresistive electrical impedance tomography (EIT) based pressure sensor can be calibrated such that applied forces in different areas can be measured.

Algorithms and Metrics Towards an Improved an Electrical Impedance Tomography Based Artificial Soft Skin Pressure Sensor

Richie Ellingham^{a,*}, Chris Pretty^a, Lui Holder-Pearson^b, Kean Aw^c, Tim Giffney^a

^a*Mechanical Engineering Department, University of Canterbury, Christchurch, 8041, Canterbury, New Zealand*

^b*Electrical and Computer Engineering Department, University of Canterbury, Christchurch, 8041, Canterbury, New Zealand*

^c*Mechanical and Mechatronics Engineering Department, University of Auckland, Auckland CBD, 1010, Auckland, New Zealand*

Abstract

Using electrical impedance tomography (EIT) to drive a pressure mapping device shows great potential, due to the customisability of the sensing domain and the non-invasive nature of the boundary electrodes. A pressure mapping system has been developed in this work that uses a silicone carbon black nanoparticle sensing domain, giving the domain with a comparable softness to human skin tissue. To take this technology into a commercial application the performance of such an EIT-based sensor must be quantifiable and repeatable. In this work a series of experiments were repeated for various load locations, strains, and carbon black percentages. Capturing this data gave insight into the how the sensing domain performs over time and captured the transient events limiting the sensor. Metrics were determined to quantify the sensor's spatial resolution. A quasi-static conductance-force model of the material was developed with an accuracy of ± 0.78 N. One important metric is temporal resolution, as it is the least quantified performance metric in literature, however can be the most important for some applications. For the sensor domains tested, average settling times of between 19.0 - 44.5 s and 22.5 - 36.0 s were determined for 8 and 9 wt% CBSR samples. A series of randomised test loads gave similar spatial performance results to the structured experiments. This sensor platform shows promise for future applications, with further materials development and processing of data the rise of an artificial biomimetic pressure sensitive skin is imminent.

Keywords: artificial skin, biocompatible, electrical impedance tomography, silicone rubber composite, soft sensors, transient phenomena, piezoresistive elastomer characterisation

1. Introduction

Approximately 1 billion years after the first animals developed mechanosensation [1], evolution has allowed humans to detect pressure through the use of many mechanoreceptors lying within the skin and other organs. Two mechanoreceptors which are desirable to emulate human touch are Merkel's disks and Meissner's corpuscles [2]. Both of which are ubiquitous in human hands and lips for high spatial resolution, low pressure and low frequency touch/pressure events [3]. These mechanoreceptors in a human hand enable object identification and closed loop fine motor control.

With the creation of pressure mapping technology which has the similar soft mechanical properties and sensing qualities to that of human skin many commercial applications requiring human-like touch could be directly fulfilled. This work presents characterisation of a soft mapping pressure sensor which utilises electrical impedance tomography to map resistance changes and subsequently stress changes throughout a soft material surface.

The number of applications that require 2D pressure sensing using a soft surface is extensive. Such applications include: robotic gripper object detection, medical mattresses and cushions, limb prostheses and wearable robotics, sport equipment, smart furniture, and rehabilitation devices. The following characteristics are desirable for each of these applications: force sensitivity, low toxicity, cost-effectiveness, repeatability, and high elasticity. In this work, a system showcasing each of these desirable characteristics has been developed.

Abbreviations: CB, carbon black; SR, silicone rubber; wt%, weight percentage; EIT, electrical impedance tomography; DUT, domain under test; PNEC, piezoresistive nanoparticle elastomer composite; ROI, region of interest; SNR, signal-to-noise ratio; CoM, centre of mass

*Corresponding author

Email address: richie.ellingham@pg.canterbury.ac.nz
(Richie Ellingham)

The sensor platform utilises a piezoresistive nanoparticle elastomer composite (PNEC) in a thin sheet topology to create an artificial sensitive skin. This artificial skin is composed of a highly elastic piezo-resistive material, and its deformation can be identified through electrical impedance tomography (EIT) for the reconstruction of the material resistivity image. Using 16 boundary electrodes, EIT facilitates the mapping of applied forces on this monolithic homogeneous material. Subsequently, an inverse model is applied to estimate compressive force loads on the material.

Understanding the electro-mechanical properties of the PNEC material is essential for creating an accurate dynamic sensor. When elastomeric composites with conductive particles, such as the PNEC, exhibit viscoelasticity, the degree of hysteresis varies based on the constituents of the composite material [4]. This viscoelasticity is a major limiting factor when using PNECs for EIT-based pressure sensing due to the frequency response lag introduced by the large transient effects seen in the material. In this work these transient phenomena are captured and characterised in the 1D and 2D compressive stress cases.

Various methods and topologies of 2D pressure mapping sensors can be employed for a 2D resistivity measurement. However, many of these methods involve intrusive and intricate electrode placement within the material domain [5, 6, 7, 8, 9, 10]. Since the materials utilised in this study are soft, the utilisation of relatively rigid metal electrodes distributed throughout the material would significantly alter the material's electromechanical deformation response. This necessitates use of the non-invasive method imaging method EIT.

1.1. EIT Background

To estimate the 2D resistivity of the PNEC a technique called electrical impedance tomography (EIT) was used. EIT allows the generation of a map of impedance values of a thin cross section of a domain under test (DUT). EIT uses a set of boundary electrodes to pass known electrical currents and measure voltages along the boundary of the DUT. From these known current injections and voltage measurements, an ill-posed inverse problem can be defined. To obtain an EIT image reconstruction three key steps are required: data acquisition, forward modelling, and inverse problem solving. A constant current can be employed to capture solely the resistance values of the DUT or as an AC signal to sweep through a range of frequencies to capture impedance data.

The forward problem in EIT is a well-posed mathematical problem, so linear algebra can be employed for obtaining electric field data for a DUT of known conductivity and a known current injection. Utilising a mesh-based coordinate system and FEM, proves to be an ef-

ficient solution for the forward model, accommodating diverse shapes. Solving the forward problem entails applying Maxwell's electromagnetic formulae to determine how an electric field would propagate through the DUT, considering the DUT conductivity. An initial estimate of the DUT resistivity is necessary for the first step of an EIT algorithm. Once the EIT forward model is solved, EIT inverse problem can be solved iteratively using the forward problem's solution. This inherently unstable problem requires optimisation algorithms and regularisation to create and linearise a solution [11, 12, 13, 14].

Once the EIT reconstruction algorithm has been tuned for an application as desired, often post-processing is completed on the reconstructed EIT image for filtering and to capture data specific for the application. A consortium of experts in the field of medicine and biomedical imaging have constructed metrics for quantifying the quality of an EIT reconstruction as shown by Adler et al. [15] and their GREIT (Graz consensus Reconstruction algorithm for EIT) performance metrics. Researchers who have used EIT pressure sensing purposes have also developed performance metrics, most of which agree with the GREIT metrics [16, 7, 17, 18, 19, 20, 21]

1.2. Related Work

Artificial skins are not a novel subject there are many different methods for localising loads in two-dimensions on a soft domain. The limiting factors found with non-EIT based methods of pressure mapping were the size discretely sensed regions, also known as sensels, is limited by various factors in the fabrication process and the bulk of electrode wires required. This bulk is exemplified high electrode-to-sensel ratio. Example load mapping technology include, optical [22, 23, 24], piezoresistive [9, 25, 26], capacitive [27], and magnetic [28]. Each of which have been compared in Table Appendix G.

Other attempts at creating artificial sensitive skins using EIT have been shown in a review by Silvera-Tawil et al. [7]. This review provides adequate evidence to display interest in the field; however, there is still no commercial EIT-based pressure sensor that is comparable in terms of spatial and temporal resolution, to commercially available non-EIT-based 2D pressure sensors. One of the earliest applications of EIT to an elastic piezo-resistive domain was achieved by Knight and Lipczynski [29] in 1990. Since this application, several other similar systems have been created using EIT and similar pressure sensitive fabrics or elastomeric materials[30, 31, 19, 7, 32, 21, 33]. A comparison of similar devices is given in Table Appendix H. None of these researched devices focus on using a material with similar softness, and quantify the stress data captured in real-time like this work. All of the referenced 'EIT' soft sensors employ electrical resistivity tomography (ERT), however, the term ERT is most commonly as-

sociated with geological subsurface imaging applications, henceforth, EIT is be used in place of ERT in this work.

2. Methodology

To substantiate the applicability of Electrical Impedance Tomography (EIT) with a monolithic PNEC sample, we fabricated the material for testing. The material needed to adhere to specific requirements: highly elastic, high yield strength, low resistivity, high piezoresistivity, non-toxic, and be a low Shore hardness of 5A - 25A akin to human soft tissue [7, 34, 35, 36]. Additionally, a system of devices was devised to facilitate EIT measurements which concurrently captured force, strain, and timestamps for each measurement. Lastly, to evaluate the sensor's suitability for diverse applications, spatial, temporal, and localised force sensing performance metrics were quantified.

2.1. Fabrication

The fabrication of the piezoresistive composite materials, as described and justified in our previous work [4], involved dispersing 8 and 9 wt% of carbon black (CB) nanoparticles in a silicone rubber (SR) matrix. Because of the difference in fabrication processes seen in literature [37, 38] and degree of dispersion generating variability in the percolation, an iterative trial and error approach using the starting point found in literature was used to get 8 wt % and 9 wt % values for CB in SR. Within this range the material was sufficiently conductive while maintaining mechanical strength through sufficient elastomeric cross-linking. Previous research indicates that there is a weight percentage at which the gauge-factor/piezoresistivity is at a maximum within a similar range used in this work [39, 40]. The composite, designated as the domain under test (DUT), was created using 50 nm average diameter XC 72R CB nanoparticles (Cabot, Alpharetta, USA) in a Dragon Skin 10 NV silicone rubber matrix (SmoothOn, Macungie, USA). Homogeneous dispersion was ensured using an ARV-310 vacuum planetary mixer (Thinky, Tokyo, Japan).

Table 1: DUT mechanical characteristics and electrical characteristics

Sample	CB wt [%]	R_{int} [$k\Omega$]	E [kPa]
SR	0	$> 1 \times 10^9$	186.16
CBSR	8	18.1 ± 9.8	132.5
CBSR	9	4.5 ± 1.4	98.1

A CBSR sample showing the circular sensitive region with the pin electrodes developed is shown in Figure 1.

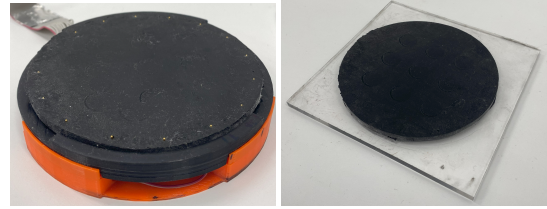


Figure 1: Left: Example of a CBSR sensing domain with gold pin electrodes penetrating material surface around the boundary on top of the rigid sensor holder (orange/black). Right: CBSR sensing domain.

2.1.1. Localised Stress Testing

Quantitative results are required for spatial quantification of the EIT image reconstructions. A cylindrical force applicator head with a diameter of 13 mm and area of 133 mm^2 was used to apply the nine compressive loads shown in Figure 2.

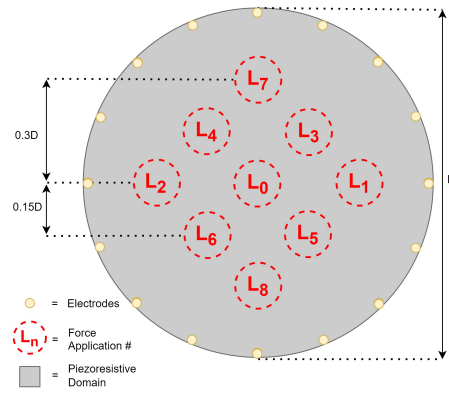


Figure 2: Load application areas used for compressive stress testing shown numerically in order of application.

2.1.2. EIT Measurement

At its core EIT usually requires a current or voltage source, one or multiple voltmeters, and a switching device. When integrating a mechanical pressure validation system a force applicator (CFA) and is also required to capture data simultaneously. The system architecture and DUT electrical connections are shown in Figure 4.

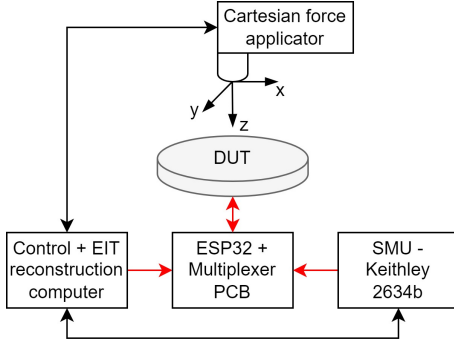


Figure 3: Architecture of the Cartesian force applicator setup with red arrows being analogue power lines and black arrows being digital data lines

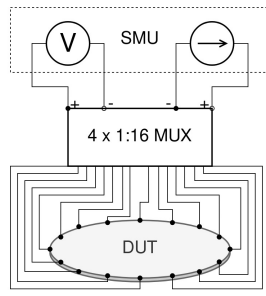


Figure 4: Wiring diagram for sensor connection to 4:16 multiplexer and SMU

2.2. 1D Material Characterisation

Prior to utilising CBSR materials as a 2D pressure sensor, the piezoresistive properties were analysed in one dimension to establish resistance-stress/strain relationships for each CBSR sample. This 1D material testing was conducted using the Cartesian force applicator in conjunction with the SMU. The stress-strain relationship of the material was determined in previous work and shown in Table 1. The 1D analysis gave quantitative insight into the material resistivity response to strain in different known areas of the Device Under Test (DUT).

2.2.1. Quasi-static Piezoresistivity

To determine the piezoresistive properties or gauge factor of the material, pin electrodes were pierced through the CBSR samples so that the pin electrodes were parallel and at a distance of 35 mm from each other. The pins were 2.5 mm from each end of the sample. A 2634b source measure unit (Keithley, Solon, USA) was used to apply a constant current of 1 mA between the two pin electrodes while ten compressive loading cycles were applied. The ten loading cycles were applied at strains of 5, 10, 15, 20, 25, and 30%, with a duty cycle of 50% and period of 120 s. Loads were applied using the Cartesian force applicator with a 20 mm x 20 mm square flat force applicator head. The

strain rate was kept at a constant $16.67\%.s^{-1}$ to dampen the amplitude of transient effects as proven in previous work [4].

When using this material to estimate stress based on resistance, any transient effects that are not correlated between resistance and stress must be accounted for. To obtain a stress reading from this PNEC CBSR material using the quasi-static model given in Equations 1 and 2, transient events were ignored, so only the steady-state conductance of the material was utilised.

$$\frac{\Delta\rho}{\rho_0} = \alpha_\sigma\sigma + \beta_\sigma \quad (1)$$

$$\frac{\Delta\rho}{\rho_0} = \alpha_\varepsilon\varepsilon + \beta_\varepsilon \quad (2)$$

Where α and β are the linear fit parameters, σ is the compressive stress, ε is the strain, $\Delta\rho$ is the change in conductance, and ρ_0 is the original material conductance.

2.2.2. Transient Piezoresistivity

There are two main piezoresistive events that occur during these compressive stress pulse response experiments. They are the compressive loading and unloading transients. Both of which result in stress relaxation and resistance relaxation behaviour until a steady-state resistance is reached. The stress relaxation can be approximated by a generalised Maxwell linear viscoelastic model [41]. A two component model was found to fit all curves without overfitting, the relaxation model from a step input is given in Equation 3.

$$G_2(t) = a_0 + a_1 e^{-t/\tau_1} + a_2 e^{-t/\tau_2} \quad (3)$$

Where $G_2(t)$ is the stress relaxation function, a_0 is the relaxation offset, a_1 & a_2 are the magnitude weightings for each time constant τ_1 & τ_2 . Equation 3 was used analogously for the resistance relaxation. To ensure repeatability of the experiment the ten loading and unloading events were fitted using equation 3 to the each relaxation, then the R^2 goodness of fit was compared for all of the relaxations.

An important temporal characteristic of this system is the settling time, t_s , given a strain step input. In this system the resistance step response settling time was the time taken to reach and stay within a specified tolerance about final steady-state resistance, given a strain step input. The tolerance chosen is about the steady state was $\pm 15\%$.

2.3. Sensor Performance Metrics

To ensure that the resistance/conductance image reconstructions which will form stress maps are valid solutions, the quality of the reconstructions needs to be quantified computationally. The purpose of this section is to describe various metrics used for sensor validation. These

metrics measure the spatial performance, temporal performance, and localised force sensing performance. Many of the spatial and temporal performance metrics have been taken and adapted from Adler et al. [15] and their GREIT (Graz consensus Reconstruction algorithm for EIT) performance metrics.

2.3.1. Pre-processing

To ascertain the occurrence of a piezoresistive event in the material, it is necessary to identify a change in resistivity that surpasses the noise floor level. This precaution is taken to differentiate between a stress compression event and potential noise artefacts. A threshold was established to eliminate the noise floor, thereby isolating the loading signal and any noise or artefacts generated by the loading signal(s).

A second threshold filter was implemented to compensate for the regularisation of the reconstruction using a percentage of the largest peak observed in the sensor image domain. The percentage threshold value used in previous work has been 25, 50, 60, 70, 75% of the maximum domain amplitude [15, 17, 7]. In this work percentage threshold masking have been applied for comparison. To validate the best percentage threshold, these thresholds were completed for a CBSR 8 and 9 wt% PNEC under nine successive loading events comparing the mean of the three main performance metrics given in Section 2.3.2. After these threshold masks have been applied to the 2D EIT images, blob(s) are observed as the sensed regions-of-interest. In this work the term 'blob' refers to an amorphous 2D shape made of several aggregated finite mesh elements. These blobs are usually observed after percentage threshold masking of an EIT image reconstruction.

2.3.2. Spatial Performance

The three main metrics of spatial performance are the centroid or centre of 'mass' error, E_{CoM} , the detected area overlap A_{OL} value, and the fit of the detected blob relative to the force input, the shape distortion, SD .

The E_{CoM} was found using:

$$E_{CoM} = \sum_i^{N_b} e_{CoM_i} \times \frac{e_i}{e_{total}} \quad (4)$$

Where N_b is the number of elements in the threshold masked blob, e_{CoM_i} is each individual element centroid, e_i is the i^{th} blob element resistance value and e_{total} is the sum of all of the blob element resistance values. This equation can be easily be inverted for images containing conductance elements in place of resistance elements. The nearer the E_{CoM} value is to zero, the better the reconstruction in regards to localising the sensed region.

The A_{OL} was found using:

$$A_{OL} = 100 \times \left[\frac{\left(\sum_i^{N_b} A_{e_i} \right)}{A_{FA}} + \frac{\left(\sum_i^{N_b} A_{e_i} \right)}{A_b} \right] / 2 : e_{CoM_i} \in \Omega_{FA} \quad (5)$$

Where A_{e_i} is the area of an element and Ω_{FA} is the domain of the force applicator area. A_{FA} and A_b are the areas of the force applicator and sensed region respectively. The closer the A_{OL} is to 100%, the better the overlap of the estimated and actual load application.

The SD was found using:

$$SD = \left[\sum_j^{N_p} \left(\|F_{CoM} - P_j\|_2 - r_{FA} \right)^2 \right] / N_p : P_j \in L_b \quad (6)$$

Where N_p is the number of mesh nodes on the perimeter of the blob, F_{CoM} is the force applicator CoM coordinates, P_j is a node in the set of blob perimetral nodes, L_b , and r_{FA} is the radius of the force applicator head. The SD is essentially the mean square error of the force applicator perimeter and sensed region perimeter taken radially from the force applicator centroid.

2.3.3. Temporal Performance

A core problem with using soft PNECs is the temporal resolution they can provide can be limited by the viscoelasticity in the material and how it interacts with the conductive network in the material. This section provides insight into how to determine the frequency response of the material, by observing the relaxation settling time of the material. The maximum time taken to reach a steady-state resistance after a stress event dictates the frequency at which the material can sense stress events. To determine the time taken to reach a steady-state, a variety of compressive stresses and strains at the loading locations, L_0-L_8 , of each DUT are observed.

To determine whether the resistance relaxation observed in the 1D case matches the relaxation of the reconstruction in 2D, the 1D and 2D relaxation settling times were compared to validate whether similar frequency responses were being observed. The EIT measurement equipment was designed such that the reconstruction frequency of 0.4 Hz can capture these transient events observed triggered in the CBSR samples, which are typically in the order of tens of seconds.

From the blob localisation described in section 2.3.2 the resistance relaxation data was extracted by plotting the sum of the blob resistance. Similar to the 1D case, the relaxations for stress loading, resistance loading, and resistance unloading scenarios are captured and compared for each CBSR with CB weight percentages of 8 and 9 wt%. The blob resistance relaxation was compared to relaxation deduced from the total image domain resistance

to ensure that the only the transient event from the area being loaded was being observed.

2.3.4. Localised Force Sensing Performance

As discussed in Section 2.2.1, a quasi-static function, Equation 1, has been generated that gives a stress based on 1D steady-state conductance measurements. This quasi-static function was applied to the DUT 2D reconstruction to obtain a stress map of the material. To determine the minimum detectable stress of the sensor the conductance noise floor values were input into the linear quasi-static Equation 1.

To obtain the stress estimate, $\hat{\sigma}_j$ and hence force estimate given a known input stress and force, the following steps were completed for each CBSR sample:

1. Determine the most likely sensed region:
 - (a) An EIT reconstruction image of a loaded DUT of a particular strain, ε_j , at a steady-state conductance was found. Each element having a change in conductance value, $\Delta\rho$, in units mS.
 - (b) Complete threshold percentage mask on image to localise the sensed region blob(s).
 - (c) The centre of mass error, E_{CoM} , between each blob and the actual force application CoM was calculated. The blob domain with the smallest E_{CoM} , Ω_s , is chosen for the following steps.
2. Equation 1 was rearranged to get an original conductance estimate for each element:

$$\rho_0 = \frac{\Delta\rho}{\alpha\sigma + \beta} \quad (7)$$

3. The mean ρ_0 and standard deviation of all of the elements in Ω_s were found.
4. Steps 1 to 3 were repeated for each strain, ε_j , applied and the mean, $\rho_0(\varepsilon_j)$ and standard deviation were calculated.
5. The mean of all $\rho_0(\varepsilon_j)$ across all strain values (i.e. $\varepsilon_j = 5, 10, 15, 20, 35, 30\%$) was calculated as $\bar{\rho}_0$.
6. $\bar{\rho}_0$ was then substituted into Equation 1 as ρ_0 , which was rearranged for stress to obtain the stress estimate as a function of mean change in conductance, $\hat{\sigma}_j(\Delta\rho_j)$, of the sensed blob domain, Ω_s .

3. Results

In the following Sections 3.1.1-3.3.2 the EIT image pre-processing, spatial, temporal, and localised force sensing performance metrics are displayed and quantified. First the steady state electrical noise, σ_n , and noise figure, NF, were determined, as given in Table 2. The NF value being a common metric showing noise amplification as a consequence of the EIT algorithm as used by Adler et al [15].

Table 2: DUT noise figure, NF, and noise, σ_n , at steady-state

CB wt%	NF	σ_n [mS]
8	1.20 ± 0.17	0.69
9	1.15 ± 0.11	0.48

3.1. 1D Material Characterisation

To generate a 2D pressure map from the EIT reconstructions a 1D material electromechanical characterisation was required. The 1D electromechanical relationship can then be extended to form an electromechanical relationship in 2D.

3.1.1. Quasi-static Piezoresistivity

Given known strain input data, and measured stress and conductance change output data, a fit is shown in Figure 5. The gradient of the linear fit, i.e. the gauge factor, for the CBSR 8 wt% and 9 wt% was calculated as 0.6 and 0.2 respectively. Note that in the 9 wt% relative conductance data the standard deviation of the 5% strain data was similar to that of the mean, hence the linear range of 10 - 30% strain was considered when fitting the curve.

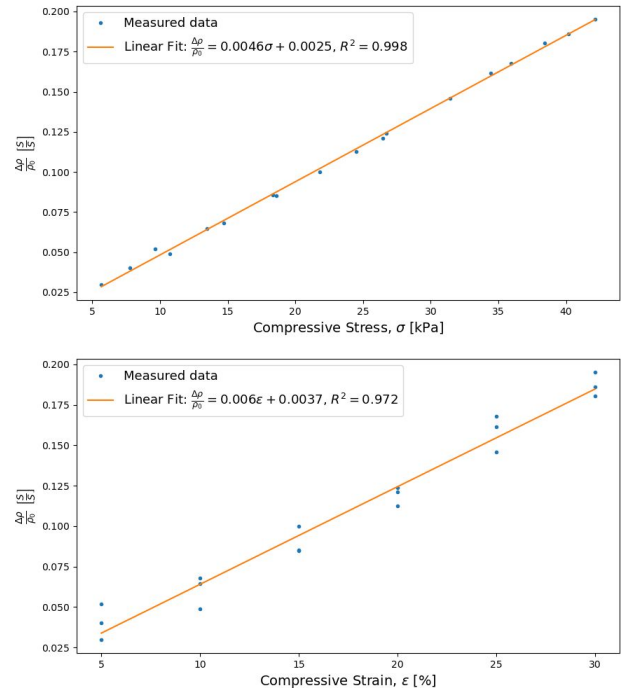


Figure 5: Conductance change vs. stress (top) and strain (bottom) data and fitted curves for 8 wt% CBSR.

3.1.2. Transient Piezoresistivity

The transient piezoresistive effects observed within a PNEC limit the frequency response of the sensor. An ex-

ample of the transient response of the material to a repeated compressive strain pulse input is displayed in Figure 6, clearly showing the stress relaxation of the material due to its viscoelasticity. In Figure 7 a loading event

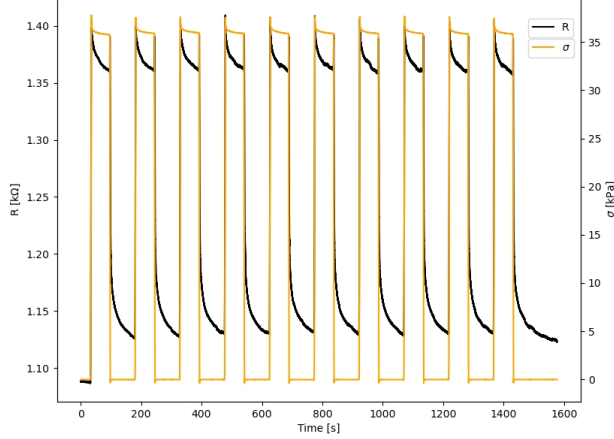


Figure 6: Compressive loading applied to the CBSR 8 wt% DUT for 10 loading events of 25% strain.

is shown with the related stress and resistance relaxation curves. The unloading event similarly has a relaxation period for both stress and resistance in the loading case. Unlike the loading stress transient, the resistance transient has a spike during the unloading relaxation event seen in Figure 7. This rising edge and peak of this spike are ignored and the resistance relaxation edge is characterised. For each stress relaxation Equation 3 was fitted to the data.

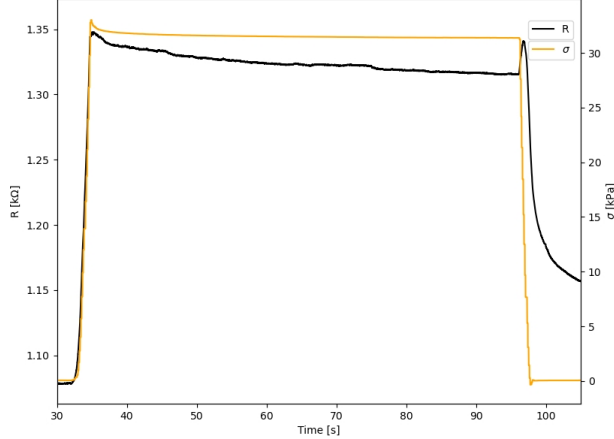


Figure 7: Compressive loading and unloading transients for CBSR 8 wt% material undergoing a 20% strain pulse from the first pulse given in Figure 6.

Analogously the same was done for the resistive relaxation events observed.

The fitted parameters were found for both 8 and 9 wt% CBSR samples, giving an indication of t

The settling times of the resistance relaxations give an indication of the frequency response of material. Thus,

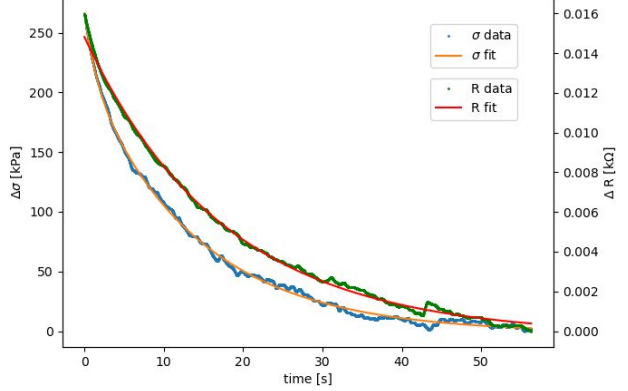


Figure 8: The fourth 1D load event, L_3 on the CBSR 8 wt% sample using 5% strain showing a stress, σ and resistance, R , relaxation event and their corresponding fitted curves.

parameters were fitted to a series of relaxations using Equation 3, then a series of fit parameters could be used to determine a mean fit. The mean fit was then used to determine the mean settling time over each ten loading events and each of the six strain values. The mean relaxation settling times were compared for each CB weight percentage as shown in Appendices D.19 and D.20.

3.2. Sensor Performance Metrics

To validate this 2D pressure sensing platform for specific applications the limits of the sensor must be known. Metrics to analyse and quantify the limits, sensor noise and spatial, temporal, and stress performance metrics are given in this section.

3.2.1. Pre-processing

The noise floor limits the detection of small forces. First the noise floor was found from the no load steady-state of material. The maximum noise from the first eight frames was found and this maximum was subtracted from all contiguous images in the time series experiment.

After a noise mask has eliminated the steady state noise floor, different percentage thresholds can be used to compensate for different regularisation and different material push area edge softness as shown in Figure B.17.

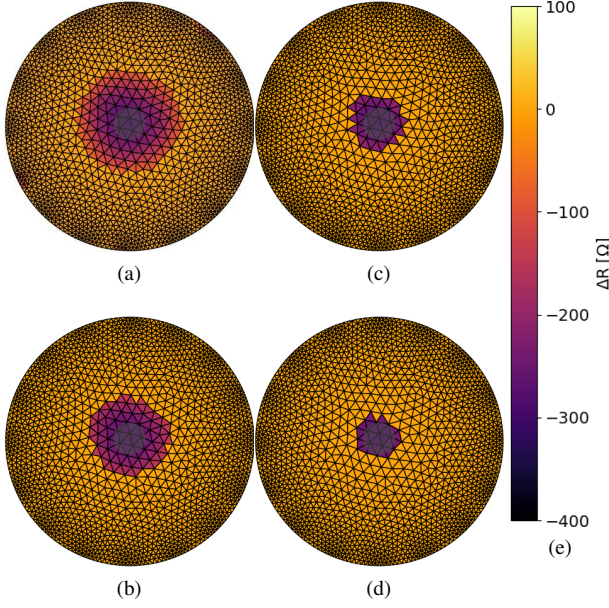


Figure 9: A series of threshold percentage masks (a) 25%, (b) 50%, (c) 75%, and (d) 85% for the same reconstruction given in Figure A.16. (e) is the resistance change scale bar.

The threshold masked image blobs and the force applicator shapes in Figures B.17a - B.17d are compared and quantified in the following section.

3.2.2. Spatial Performance

To properly determine where the perimeter of a load is multiple threshold mask filters were applied. To validate the threshold mask percentages the three main performance characteristics were displayed as separate time series for each material, each applied strain, and each threshold percentage mask. These time series show how each metric changed over the course of a loading test sequence and how the metrics vary across the surface of the DUT. An example comparing this time series data for two instances where a 20% strain pulse train was applied to a the nine loading locations with multiple threshold mask percentages is shown in Figures 10 and Appendix E.23 for for 8 and 9 wt% CBSR samples respectively.

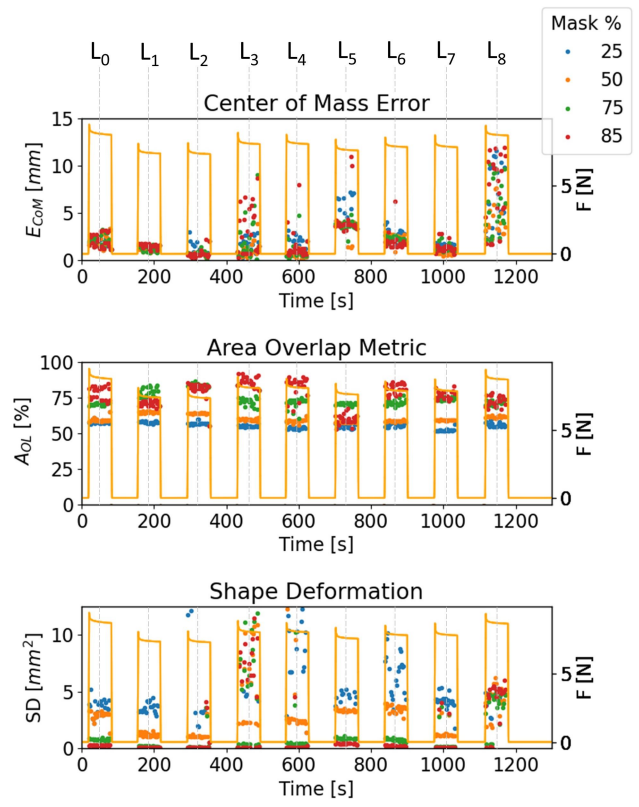


Figure 10: Spatial performance metrics comparing threshold percentages of 25, 50, 75, and 85% for a 8 wt% CBSR sample being loaded with 20% compressive strain in nine areas, L_0 - L_8 , shown in Figure 2. The force time series plot data is light orange.

The percentage threshold masks from 25 - 85% were compared by finding the mean of all of the spatial performance metrics for each strain from 5 - 30%. The mean and standard deviation for each of these metrics from the data shown in Figure 10 is given in Tables 3 and 4.

Table 3: CBSR 8 wt% mean and standard deviation for spatial performance metrics across of a nine loads, L_0 - L_8 and strain value 20%.

% thresh	E_{CoM} [mm]	A_{OL} [%]	SD [mm^2]
0.25	4.1 ± 6.3	53.3 ± 15.3	10.4 ± 9.3
0.5	3.3 ± 6.3	57.5 ± 16.3	3.6 ± 4.4
0.75	3.8 ± 6.3	69.6 ± 19.8	2.4 ± 5.8
0.85	4.1 ± 6.4	72.5 ± 21.7	2.4 ± 6.5

Table 4: CBSR 8 wt% mean and standard deviation for spatial performance metrics of nine loads, L_0 - L_8 , a 85% percentage threshold mask, and strain value 20%.

Load	E_{CoM} [mm]	A_{OL} [%]	SD [mm 2]
L_0	2.05 ± 0.70	80.39 ± 4.19	0.28 ± 0.01
L_1	1.53 ± 0.23	72.32 ± 1.74	0.12 ± 0.01
L_2	0.67 ± 0.41	83.00 ± 2.38	0.48 ± 1.16
L_3	3.29 ± 2.17	87.93 ± 2.68	5.25 ± 3.78
L_4	1.44 ± 1.61	84.81 ± 5.78	2.76 ± 5.65
L_5	4.43 ± 2.09	61.08 ± 3.29	7.39 ± 16.31
L_6	2.03 ± 1.05	82.19 ± 3.55	3.14 ± 8.57
L_7	1.49 ± 0.56	77.68 ± 2.46	0.66 ± 1.25
L_8	6.95 ± 3.67	73.69 ± 3.60	3.78 ± 2.01

3.3. Randomised Location and Strain Testing

In a real world application the sensor platform in this work will likely experience a large range of unknown loads in various locations. To ensure that the device operates in a similar fashion to that seen in the structured experimental data, a randomised experiment was completed. The randomised experiment loads were at ten randomised radii, r_{rand} , angles, θ_{rand} , and strain values, within the ranges, 0 - 40% of the domain radius, 0 - 360°, and 5 - 30% respectively.

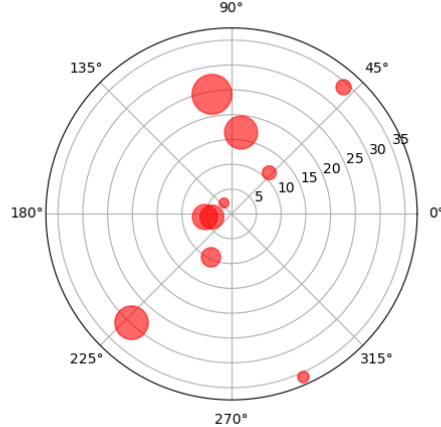


Figure 11: The ten random load point locations, L_{rand} and random strain values proportional to rec circle size as shown on a polar plot.

Spatial performance metrics for these tests are given in Tables 5 and F.6 with the load points and their magnitudes shown diagrammatically in Figure 11. A pseudo-random number generator with a uniform distribution was used for all randomly generated data.

Table 5: CBSR 8 and 9 wt% mean and standard deviation for E_{CoM} spatial performance metrics of ten random locations, L_{rand} and random strains ε

L_{rand} (r , θ) [mm, °]	ε [%]	8wt% E_{CoM} [mm]	9wt% E_{CoM} [mm]
(5.4, 10)	17.9	3.1 ± 0.7	3.1 ± 0.5
(29.8, 337)	24.0	1.9 ± 0.4	5.0 ± 0.6
(4.2, 317)	17.0	7.9 ± 2.2	9.0 ± 1.0
(34.0, 70)	10.9	6.0 ± 3.5	2.9 ± 0.5
(35.8, 137)	8.1	13.9 ± 0.6	7.7 ± 4.6
(9.6, 55)	13.8	6.0 ± 1.0	10.3 ± 4.4
(2.8, 260)	7.0	12.0 ± 8.1	28.7 ± 10.9
(11.2, 114)	10.0	5.1 ± 1.2	12.0 ± 1.9
(24.6, 241)	28.5	2.3 ± 0.2	2.4 ± 0.2
(16.6, 253)	23.6	3.1 ± 0.4	7.1 ± 0.5

3.3.1. Temporal Performance

Temporal performance is crucial for time sensitive applications and the settling time of the sensing material domain must be known to apply a quasi-static force model. The fitted stress and resistance relaxation parameters were found for both 8 and 9 wt% CBSR samples, giving an indication of the frequency response of material across all experiments. To ensure a good fit all fits with an R^2 value less than 0.85 were eliminated.

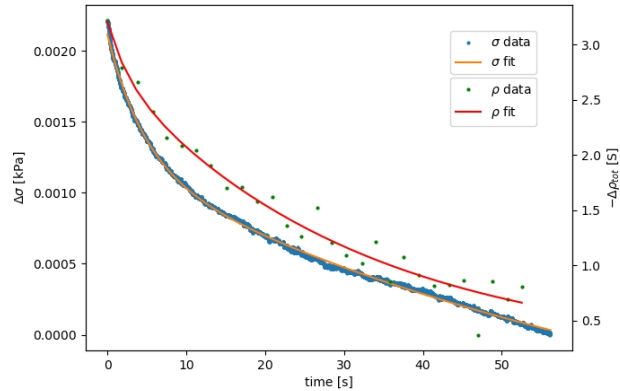


Figure 12: EIT load event L_0 on the CBSR 9 wt% sample using 30% strain showing a stress, σ and conductance, ρ , relaxation event and their corresponding fitted curves.

The mean settling time for each strain was calculated across relaxations for all strains, all 9 locations, and all 3 trials. The settling times were compared for each CB weight percentage as shown in Appendices D.21 and D.22.

3.3.2. Localise Force Sensing Performance

To determine the localised force sensing performance the linear quasi-static Equation 1 was applied to the percentage threshold masked image blobs developed in section 2.3.2.

To determine the force sensing limits of the material, the force estimated erroneously due to the EIT reconstruction noise floor must be determined. The noise floor is the noise observed over a time series of EIT images when the DUT has zero load applied and there are no resistive transient effects present. The noise floor, $\Delta\rho_n$, of unloaded relaxed 8 and 9 wt% CBSR DUT conductance images were calculated as ± 0.33 and $\pm 0.34 \mu\text{S}$ respectively. An average DUT inter-electrode conductance, ρ_{int} , of 55.3 and $222.2 \mu\text{S}$ was derived from Table 1 for CBSR 8 and 9 wt% respectively. A relative change of conductance value, $\frac{\Delta\rho_n}{\rho_{int}}$, was then calculated as 5.97×10^{-3} and $1.53 \times 10^{-3} \mu\text{S}$ for CBSR 8 and 9 wt% respectively. From the quasi-static piezoresistivity Equation 1 and the fitted quasi-static piezoresistivity parameters found in Section 3.1.1, we calculated the mean force approximation error as 0.17 N for both CBSR 8 and 9 wt%.

The force estimation from the inverse quasi-static Equation 1 was compared to the actual force loaded onto the DUT as measured by the force applicator loadcell. Figures 13 and 14 show data from load applications in the centre (L_0) of the respective 8 and 9wt% CBSR DUTs with a force estimation standard deviation of ± 0.78 and $\pm 0.81 \text{ N}$ respectively.

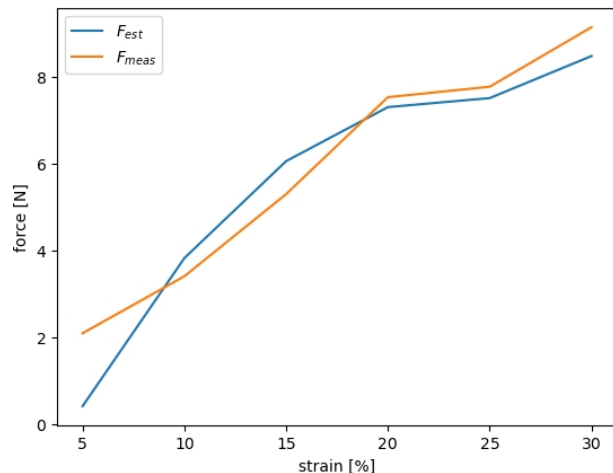


Figure 13: Comparing force estimates, F_{est} , and actual force measurements, F_{meas} , for 5 - 30% strain centre loading events at L_0 for the EIT sensor system for 8 wt% CBSR

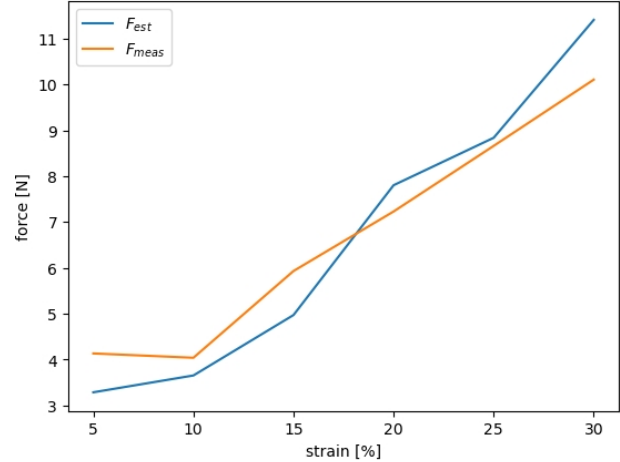


Figure 14: Comparing force estimates, F_{est} , and actual force measurements, F_{meas} , for 5 - 30% strain centre loading events at L_0 for the EIT sensor system for 9 wt% CBSR

4. Discussion

Potential applications that emulate human-like skin pressure sensing characteristics require a forms of quantification to compare the technology to the specific requirements. This work quantitatively characterises performance metrics to help facilitate that comparison and optimisation process. The sensor developed could be likened to slow acting mechanoreceptors within human skin, such as Meissner's corpuscles and Merkel's discs, which combined can detect static pressure, and high resolution touch. For other EIT-based pressure mapping applications to be realised, the metrics developed in this work are some of the core metrics required to determine which soft sensing domains are suitable and are their limits.

4.1. Quasi-static Piezoresistivity

To make a low-frequency response load sensor, a quasi-static piezoresistive linear model was created as shown in Section 3.1. However, this model is only valid for sufficiently slow pressure applications or after a sufficiently long time period. This time period is determined by the largest expected steady-state relaxation time for the material shown in 3.1.1

4.2. Pre-processing

The two steps of a noise threshold mask and a percentage threshold mask successfully filtered noise and EIT reconstruction related noise artefacts. The favoured percentage threshold mask chosen for further metrics testing was 85% as this gave the lowest average E_{CoM} and SD values from the across all strains applied across all nine loading points.

In the experiments often a blob detection from a previous load will be present in a subsequent load, as expected

due to the resistive relaxation. Feature detection could be added in future to ensure that only transients similar to those seen in the initial formation of a blob would signify that the blob is to be analysed. Concurrently, each blob could be tracked individually to determine whether it is a noise artefact or an actual sensed region depending on its behaviour.

4.3. Performance Metrics

To develop sensing domains for future applications, the sensing domains may need take into account certain prior information about the limits of the system.

For example, human hands and feet have some of the highest density of mechanoreceptors in the body. Lower density regions of mechanoreceptors in humans include the back and chest [2]. Higher spatial resolution is required for emulating the pressure mapping of a human hands and feet, compared to the human back and chest. However, the pressure sensing range required by the human hands may be lower than that required by the human feet.

Using this prior information, we can validate the appropriate sensing domain characteristics that give a suitable performance for each different application.

Depending on the application of the sensor the importance of each temporal, spatial, and force sensing performance metrics could all vary.

4.3.1. Spatial Performance

All spatial performance metrics, E_{CoM} , A_{OL} , and SD are key indicators of whether a loading event has been localised correctly.

The A_{OL} gives a value out of 100 for a certain detected blob. This value is penalised for false positive and true negative elements that overlap (or not) with the force applicator area.

It is important to note, when a force is applied in a small area of a domain, however a blob has been detected over the majority area of the domain, a A_{OL} value of $\leq 50\%$ will be given although the blob detection could be completely false. Although the detected blob and force applicator are 100% overlapping the amount of false positive (i.e. blob elements not overlapping with force applicator area) could cover the rest of the DUT, potentially giving a value nearer to 50% than 0%. From this it must be recognised that this metric does not represent a linear relationship between A_{OL} and the quality of the reconstruction. So the scale of the A_{OL} value to quality relationship was determined empirically as:

$$0 \leq A_{OL} \leq 50\% = \text{Likely Poor}$$

$$50 \leq A_{OL} \leq 70\% = \text{Ok}$$

$$70 \leq A_{OL} \leq 100\% = \text{Good}$$

The SD is the mean square error between the force applicator perimeter and sensed region perimeter taken radially from the force applicator centroid, so will likely be lower with a low E_{CoM} and a higher A_{OL} . The closer the SD value is to zero the more accurately the shape of the load area applied has been sensed. The SD metric is also affected significantly by the quantisation error depending on the mesh coarseness.

Comparing the different percentage threshold masks for the experiment shown in Figure 10, it was determined that each percentage mask of 50%, 75%, and 85% gave showed the spatial performance for the E_{CoM} , SD , and A_{OL} . However, the standard deviation of these values is comparable to the mean itself therefore looking at the mean performance metric value in each location was shown in Table 4. The lowest E_{CoM} was found to be 0.67 ± 0.41 mm, at L_2 . The highest A_{OL} value was found to be $87.93 \pm 2.68\%$. The lowest SD value was found to be 0.12 ± 0.01 mm 2 at L_1 .

The CBSR 8 wt% samples gave better performance metric results than the 9 wt% samples due to the residual transient effects of previous load events as exemplified in Figure E.23. This will be mitigated in future by using a blob separation algorithm whereby each sensed-region/blob is given a weighting based on its appearance time, size, decay characteristic, and performance metric values.

The spatial performance metrics are useful for quantifying future testing with irregular load application area shapes and multiple loading events in future testing to validate a variety of irregular and multi-load test cases. Performance metric inconsistencies in the different load locations show that the electro-mechanical characteristics of the material varies throughout the material. These metrics would all contribute toward a calibration step to compensate for material inhomogeneity, allowing for a range of materials to be used for the sensing domain.

4.3.2. Temporal Performance

Many applications require a minimum frequency response hence a temporal study was completed to characterise the transient effects limiting the speed of the sensor. The study focused on the settling time of transient piezoresistive events in the material for varying strain step inputs. With known PNEC material settling times, a filter could be applied to the output of this sensor to get an estimate of the load applied to the material.

To aid future inverse modelling and use of PNECs as pressure sensor it is important to understand each transient states of a load, including the loading phase, steady state, or unloading phase. It was found that on average that unloading events had a higher settling time than loading transients for both CBSR 8 and 9 wt% composites across all strains tested from 5 to 30%. No clear correla-

tion was found between the settling time of the transient strain events and the strain percentage applied to the material. Mean settling times ranging 29 - 36 s and 29 - 41 s have been observed for the CBSR 8 and 9 wt% composites respectively.

A different sensing region material could provide a higher frequency response, such as a carbon nanotube silicone composite which has shown a lower settling time in previous works [42, 43]. Due to the viscoelasticity and elastic rebound in the material the resistance relaxation from predeccesing load applications was often present in subsequent load events, altering the observed resistance relaxation response. Future algorithms developed would aim to eliminate these predeccesing residual relaxations.

Often soft materials are inherently viscoelastic like much soft tissue within the human body [36], so if soft sensor domains are required with a high frequency response this viscoelasticity will need to be compensated for using this work's performance metrics as a foundation.

It is important to note that if the homogeneity in the material is highly irregular, regions of the material will have different degrees of piezoresistivity the frequency response of the material is likely to vary considerably. Further research is required into how the different CB wt % values effect the temporal response of the material.

4.3.3. Localised Force Sensing Performance

The sensor platform gave stress estimates that correlated well with the real stress applied to the material, as seen in Figures 13 and 14. These stress estimates were gathered from the steady-state data gathered from the EIT measurements at approximately 1.5x the settling times found in Section 3.3.1 using the algorithm given in Section 3.3.2 to ensure the data was at steady state.

Stress relaxation of the composite CBSR material as a whole gives a good indication of macro-mechanical behaviour of the CBSR. It was postulated that the resistance relaxation gives an enhanced insight into the micro(and nano)-structural behaviour of the CBSR composite, because of the different observed behaviours of the CBSR stress and resistive relaxation and also how these relate to different CB weight percentages and their dispersion.

4.4. Real World Applications, Manufacturability, and Scalability

Using EIT-based pressure mapping on a larger scale is feasibly as shown by the use of ERT in geophysics [44]. Potential larger-scale applications include adding a pressure mapping layer under a tennis court to map force exerted by athletes onto a court or a method of measuring foot traffic in buildings and urban areas. The use of the performance metrics discussed in this work would be applicable for both scenarios.

For the tennis court application, the importance of player location and speed may be more important than detecting the footprint shape and exact force applied to the court surface. This means that the E_{CoM} and decay time values would be more heavily weighted than the SD and force values, and hence could be tuned for these characteristics. For the urban floor mat application, the importance of footprint shape and force estimation may give useful insight into the physical demographic of people or animals walking across the mat [45]. This may mean that the SD and force resolution values are more highly weighted in the design and process.

Larger-scale applications of an EIT-based sensor come with challenges such as, scaling the electronics driving the EIT measurement, fabricating such a large homogeneously piezoresistive domain, and ensuring the reliability in a range of outdoor environmental conditions. Smaller-scale applications are limited by the conductive particle size in the PNEC. A sensing domain thickness sufficiently larger than the average agglomerate size would be required for reliable EIT mapping and force estimates.

Various forms of tribological wear on the device sensing region would alter the piezoresistive characteristic of the device. Encapsulation of the device could be implemented to minimise wear and increase hermeticity.

The most obvious limitation of this sensor is the frequency response of the material as shown in Figures D.19 - D.22, which could be algorithmically filtered or inverse-modeled to be corrected. Else, other more responsive, less viscoelastic materials could be used, and/or a capacitive EIT-based pressure mapping device used to improve the frequency response of this device. Otherwise the use of a time series dependent neural network, such as an LTSM, RNN, could be used to inversely model such events.

Mass production of an EIT-based sensor would use the performance metrics given in this work to calibrate and quality-check the sensing domain and boundary electrode connections. This work also found that using pin boundary electrodes adds to the durability and stability of electrical connection in this device.

5. Summary and Conclusions

An EIT-based piezoresistive sensor using a custom made carbon black silicone rubber composite material has been developed for sensing compressive pressure events and applying performance metrics to obtain the validity of the output EIT images. To be able to apply this EIT-based PNEC pressure sensor to a variety of scenarios, replacing human-like touch, performance metrics has been formed to quantify the sensor's suitability for each application. Sensing domains of 8 and 9 wt% carbon black silicone rubber have been tested using: 6 strain values, 9 load locations, and 3 trials. From this raw data we have

calculated data for: spatial resolution, transient settling time, and force sensor resolution.

It was shown that the CBSR 8 wt% sample out performed the CBSR 8wt% sample in terms of spatial and temporal metrics across a range of experiments. The best performance metrics observed in the CBSR 8 wt% sample for E_{CoM} , A_{OL} , and SD , were 0.67 ± 0.41 mm, $87.93 \pm 2.68\%$, and 0.12 ± 0.01 mm 2 respectively for three different load locations. For the sensor domains tested, average settling times of between 19.0 - 44.5 s and 22.5 - 36.0 s were determined for 8 and 9 wt% CBSR samples. A quasi-static conductance-force model of the material was developed with an accuracy of ± 0.78 and ± 0.81 N for a range of strains from a centre load test for 8 and 9 wt% CBSR respectively.

Using these performance metric data in future work a piezoresistively inhomogeneous sensor domain could be, calibrated to homogenise the apparent domain piezoresistivity, compensated for transient phenomena, and sense loads with a known degree of accuracy. All of these factors contribute to optimising the EIT-based 2D pressure mapping sensor for different applications. Future work also includes the development of a low-cost, small circuit to capture the the data discretely to open up a larger range of applications. The work shows promise for future use of an EIT-based sensor in a variety of applications requiring a soft sensing domain and non-invasive rigid electrodes.

References

- [1] L. W. Parfrey, D. J. Lahr, A. H. Knoll, L. A. Katz, Estimating the timing of early eukaryotic diversification with multigene molecular clocks, *Proceedings of the National Academy of Sciences of the United States of America* 108 (2011) 13624–13629. URL: [/pmc/articles/PMC3158185/](https://www.ncbi.nlm.nih.gov/pmc/articles/PMC3158185/)?report=abstracthttps://www.ncbi.nlm.nih.gov/pmc/articles/PMC3158185/. doi:10.1073/PNAS.1110633108/-/DCSUPPLEMENTAL.
- [2] K. Andre, I. Kiseleva, *Mechanosensitivity of the Nervous System*, 1 ed., Springer Dordrecht, 2008.
- [3] C. Molnar, J. Gair, *Somatosensation*, 1 ed., Open-TextBC, 2015. URL: <https://opentextbc.ca/biology/chapter/17-2-somatosensation/>.
- [4] R. Ellingham, T. Giffney, Stress and Resistance Relaxation for Carbon Nanoparticle Silicone Rubber Composite Large-Strain Sensors, Volume 7: 17th IEEE/ASME International Conference on Mechatronic and Embedded Systems and Applications (MESA) (2021). URL: <https://asmedigitalcollection.asme.org/IIDETC-CIE/proceedings/IIDETC-CIE2021/85437/V007T07A046/1128153>. doi:10.1115/DETC2021-69206.
- [5] B. F. Gonçalves, J. Oliveira, P. Costa, V. Correia, P. Martins, G. Botelho, S. Lanceros-Mendez, Development of water-based printable piezoresistive sensors for large strain applications, *Composites Part B: Engineering* 112 (2017) 344–352. doi:10.1016/J.COMPOSITESB.2016.12.047.
- [6] P. Loew, M. Brill, G. Rizzello, S. Seelecke, Development of a nonintrusive pressure sensor for polymer tubes based on dielectric elastomer membranes, *Sensors and Actuators A: Physical* 292 (2019) 1–10. doi:10.1016/J.SNA.2019.03.006.
- [7] D. Silvera-Tawil, D. Rye, M. Soleimani, M. Velonaki, Electrical impedance tomography for artificial sensitive robotic skin: A review, *IEEE Sensors Journal* 15 (2015) 2001–2016. doi:10.1109/JSEN.2014.2375346.
- [8] J. Lee, J. Kim, Y. Shin, I. Jung, Ultra-robust wide-range pressure sensor with fast response based on polyurethane foam doubly coated with conformal silicone rubber and CNT/TPU nanocomposites islands, *Composites Part B: Engineering* 177 (2019) 107364. doi:10.1016/J.COMPOSITESB.2019.107364.
- [9] G. Gilanizadehdizaj, K. C. Aw, J. Stringer, D. Bhattacharyya, Facile fabrication of flexible piezo-resistive pressure sensor array using reduced graphene oxide foam and silicone elastomer, *Sensors and Actuators A: Physical* 340 (2022) 113549. doi:10.1016/J.SNA.2022.113549.
- [10] Y. Zhu, K. Aw, T. Giffney, Dielectric elastomer-based multi-location capacitive sensor, 2021. URL: <https://researchspace.auckland.ac.nz/handle/2292/60603>.
- [11] R. Bayford, Basic Electrical Impedance Tomography, in: *Bioimpedance in Biomedical Applications and Research*, Springer, Cham, 2018, pp. 29–44. URL: https://link.springer.com.ezproxy.canterbury.ac.nz/chapter/10.1007/978-3-319-74388-2_3. doi:10.1007/978-3-319-74388-2_3.
- [12] W. R. B. Lionheart, EIT Reconstruction Algorithms: Pitfalls, Challenges and Recent Developments, *Physiological Measurement* 25 (2003) 125–142. URL: <http://arxiv.org/abs/physics/0310151http://dx.doi.org/10.1088/0967-3334/25/1/021>.

- doi:10.1088/0967-3334/25/1/021.
arXiv:0310151v2.
- [13] T. de Castro Martins, A. K. Sato, F. S. de Moura, E. D. L. B. de Camargo, O. L. Silva, T. B. R. Santos, Z. Zhao, K. Möller, M. B. P. Amato, J. L. Mueller, R. G. Lima, M. de Sales Guerra Tsuzuki, A review of electrical impedance tomography in lung applications: Theory and algorithms for absolute images, *Annual Reviews in Control* 48 (2019) 442–471. doi:10.1016/J.ARCONTROL.2019.05.002.
- [14] A. Adler, D. Holder, *Electrical Impedance Tomography*, 2 ed., CRC Press, 2021. doi:10.1201/9780429399886.
- [15] A. Adler, J. H. Arnold, R. Bayford, A. Borasic, B. Brown, P. Dixon, T. J. Faes, I. Frerichs, H. Gagnon, Y. Gärber, B. Grychtol, G. Hahn, W. R. Lionheart, A. Malik, R. P. Patterson, J. Stocks, A. Tizzard, N. Weiler, G. K. Wolf, Greit: a unified approach to 2d linear eit reconstruction of lung images, *Physiological measurement* 30 (2009). URL: <https://pubmed.ncbi.nlm.nih.gov/19491438/>. doi:10.1088/0967-3334/30/6/S03.
- [16] S. Wang, T. Kaaya, Z. Chen -, T. N. Tallman, D. J. Smyl, Structural health and condition monitoring via electrical impedance tomography in self-sensing materials: a review, *Smart Materials and Structures* 29 (2020) 123001. URL: <https://iopscience.iop.org/article/10.1088/1361-665X/abb352><https://iopscience.iop.org/article/10.1088/1361-665X/abb352/meta>. doi:10.1088/1361-665X/ABB352.
- [17] F. Visentin, P. Fiorini, K. Suzuki, A deformable smart skin for continuous sensing based on electrical impedance tomography, *Sensors* 2016, Vol. 16, Page 1928 16 (2016) 1928. URL: <https://www.mdpi.com/1424-8220/16/11/1928><https://www.mdpi.com/1424-8220/16/11/1928>. doi:10.3390/S16111928.
- [18] T. N. Tallman, D. J. Smyl, Structural health and condition monitoring via electrical impedance tomography in self-sensing materials: a review, *Smart Materials and Structures* 29 (2020) 123001. URL: <https://iopscience.iop.org/article/10.1088/1361-665X/abb352><https://iopscience.iop.org/article/10.1088/1361-665X/abb352/meta>. doi:10.1088/1361-665X/ABB352.
- [19] L. Sun, S. Jiang, Y. Xiao, W. Zhang, Realization of flexible pressure sensor based on conductive polymer composite via using electrical impedance tomography, *Smart Materials and Structures* 29 (2020) 055004. URL: <https://iopscience-iop-org.ezproxy.canterbury.ac.nz/article/10.1088/1361-665X/ab75a3><https://iopscience-iop-org.ezproxy.canterbury.ac.nz/article/10.1088/1361-665X/ab75a3/meta>. doi:10.1088/1361-665X/AB75A3.
- [20] A. Hassan, A. Nagakubo, Y. Kuniyoshi, A tactile distribution sensor which enables stable measurement under high and dynamic stretch, *3DUI - IEEE Symposium on 3D User Interfaces 2009 - Proceedings* (2009) 87–93. doi:10.1109/3DUI.2009.4811210.
- [21] Y. Kato, T. Mukai, T. Hayakawa, T. Shibata, Tactile sensor without wire and sensing element in the tactile region based on EIT method, *Proceedings of IEEE Sensors* (2007) 792–795. doi:10.1109/ICSENS.2007.4388519.
- [22] M. Ramuz, B. C. Tee, J. B. Tok, Z. Bao, Transparent, optical, pressure-sensitive artificial skin for large-area stretchable electronics, *Advanced Materials* 24 (2012) 3223–3227. URL: <https://onlinelibrary.wiley.com/doi/full/10.1002/adma.201200523><https://onlinelibrary.wiley.com/doi/abs/10.1002/adma.201200523><https://onlinelibrary.wiley.com/doi/10.1002/adma.201200523>. doi:10.1002/ADMA.201200523.
- [23] S. Shimadera, K. Kitagawa, K. Sagehashi, Y. Miyajima, T. Niizyama, S. Sunada, Speckle-based high-resolution multimodal soft sensing, *Scientific Reports* 2022 12:1 12 (2022) 1–11. URL: <https://www.nature.com/articles/s41598-022-17026-0>. doi:10.1038/s41598-022-17026-0.
- [24] J. Rossiter, T. Mukai, A novel tactile sensor using a matrix of leds operating in both photoemitter and photodetector modes, *Proceedings of IEEE Sensors* 2005 (2005) 994–997. doi:10.1109/ICSENS.2005.1597869.
- [25] Y. F. Fu, F. L. Yi, J. R. Liu, Y. Q. Li, Z. Y. Wang, G. Yang, P. Huang, N. Hu, S. Y. Fu, Super soft but strong e-skin based on carbon fiber/carbon black/silicone composite: Truly mimicking tactile sensing and mechanical behavior of human skin, *Composites Science and Technology* 186 (2020) 107910. doi:10.1016/J.COMPSCITECH.2019.107910.

- [26] K. . Yang, X. . Xia, F. . Zhang, H. . Ma, S. . Sang, Q. . Zhang, J. Ji, K. Yang, X. Xia, F. Zhang, H. Ma, S. Sang, Q. Zhang, J. Ji, Implementation of a Sponge-Based Flexible Electronic Skin for Safe Human–Robot Interaction, *Micromachines* 13 (2022) 1344. URL: <https://www.mdpi.com/article/10.3390/mi13081344>. doi:10.3390/mi13081344.
- [27] G. Liang, Y. Wang, D. Mei, K. Xi, Z. Chen, Flexible capacitive tactile sensor array with truncated pyramids as dielectric layer for three-axis force measurement, *Journal of Microelectromechanical Systems* 24 (2015) 1510–1519. doi:10.1109/JMEMS.2015.2418095.
- [28] Y. Yan, Z. Hu, Z. Yang, W. Yuan, C. Song, J. Pan, Y. Shen, Soft magnetic skin for super-resolution tactile sensing with force self-decoupling, *Science Robotics* 6 (2021) 8801. URL: <https://www.science.org/doi/10.1126/scirobotics.abc8801>. doi:10.1126/SCIROBOTICS.ABC8801/SUPPLFILE/ABC8801_SM.PDF.
- [29] R. Knight, R. Lipczynski, The Use Of Eit Techniques To Measure Interface Pressure, in: Annual International Conference of the IEEE Engineering in Medicine and Biology Society, Institute of Electrical and Electronics Engineers (IEEE), 1990, pp. 2307–2308. URL: <https://doi-org.ezproxy.canterbury.ac.nz/10.1109/IEMBS.1990.692299>. doi:10.1109/IEMBS.1990.692299.
- [30] A. Nagakubo, H. Alirezaei, Y. Kuniyoshi, A deformable and deformation sensitive tactile distribution sensor, 2007 IEEE International Conference on Robotics and Biomimetics, ROBIO (2007) 1301–1308. doi:10.1109/ROBIO.2007.4522352.
- [31] S. Russo, S. Nefti-Meziani, N. Carbonaro, A. Tognetti, A Quantitative Evaluation of Drive Pattern Selection for Optimizing EIT-Based Stretchable Sensors, *Sensors* 17 (2017). URL: www.mdpi.com/journal/sensors. doi:10.3390/s17091999.
- [32] S. H. Yoon, K. Huo, Y. Zhang, G. Chen, L. Paredes, S. Chidambaram, K. Ramani, iSoft: A Customizable Soft Sensor with Real-time Continuous Contact and Stretching Sensing, Proceedings of the 30th Annual ACM Symposium on User Interface Software and Technology (2017) 665–678. URL: [https://doi.org/10.1145/3126594](https://doi.org/10.1145/3126594.3126654). doi:10.1145/3126594.
- [33] N. Biasi, A. Gargano, L. Arcarisi, N. Carbonaro, A. Tognetti, Physics-based Simulation and Machine Learning for the Practical Implementation of EIT-based Tactile Sensors, *IEEE Sensors Journal* (2022). doi:10.1109/JSEN.2022.3144038.
- [34] P. E. Chatzistergos, D. Allan, N. Chockalingam, R. Naemi, Shore hardness is a more representative measurement of bulk tissue biomechanics than of skin biomechanics., *Medical Engineering Physics* 105 (2022) 103816. doi:10.1016/J.MEDENGPHY.2022.103816.
- [35] B. McDermott, B. McGinley, K. Kruckiewicz, B. Divilly, M. Jones, M. Biggs, M. O'Halloran, E. Porter, Stable tissue-mimicking materials and an anatomically realistic, adjustable head phantom for electrical impedance tomography, *Biomedical Physics Engineering Express* 4 (2017) 015003. URL: <https://iopscience.iop.org/article/10.1088/2057-1976/aa922d>. doi:10.1088/2057-1976/AA922D.
- [36] G. Landry, K. Parodi, J. E. Wildberger, al, M. Simard, A. Lalonde, H. Bouchard, G. Singh, A. Chanda, Mechanical properties of whole-body soft human tissues: a review, *Biomedical Materials* 16 (2021) 062004. URL: <https://iopscience.iop.org/article/10.1088/1748-605X/ac2b7a>. doi:10.1088/1748-605X/AC2B7A.
- [37] M. E. D'Asaro, M. S. Otten, S. Chen, J. H. Lang, Multidimensional characterization of piezoresistive carbon black silicone rubber composites, *Journal of Applied Polymer Science* 134 (2017). URL: <http://doi.wiley.com/10.1002/app.44773>. doi:10.1002/app.44773.
- [38] S. Shang, Y. Yue, X. Wang, Piezoresistive strain sensing of carbon black /silicone composites above percolation threshold, *Review of Scientific Instruments* 87 (2016) 123910. URL: [/aip/rsi/article/87/12/123910/916719/Piezoresistive-strain-sensing-of-carbon-black](https://aip/rsi/article/87/12/123910/916719/Piezoresistive-strain-sensing-of-carbon-black). doi:10.1063/1.4973274/916719.
- [39] S. Dong, X. Wang, Alignment of carbon iron into polydimethylsiloxane to create conductive composite with low percolation threshold and high piezoresistivity: experiment and simulation, *Smart Materials and Structures* 26 (2017) 045027. URL:

- <https://iopscience-iop-org.ezproxy.canterbury.ac.nz/article/10.1088/1361-665X/aa62d2>
<https://iopscience-iop-org.ezproxy.canterbury.ac.nz/article/10.1088/1361-665X/aa62d2/meta>
doi:10.1088/1361-665X/AA62D2.
- [40] H. Yang, L. H. Gong, Z. Zheng, X. F. Yao, Highly stretchable and sensitive conductive rubber composites with tunable piezoresistivity for motion detection and flexible electrodes, *Carbon* 158 (2020) 893–903. URL: <http://www.sciencedirect.com/science/article/pii/S0008622319312126>. doi:<https://doi.org/10.1016/j.carbon.2019.11.079>.
- [41] Y. C. Ju, D. Chiang, M. Y. Tsai, H. Ouyang, S. Lee, Stress Relaxation Behavior of Poly(Methyl Methacrylate)/Graphene Composites: Ultraviolet Irradiation, *Polymers* 14 (2022). doi:[https://doi.org/10.3390/POLYM14194192/S1](https://doi.org/10.3390/POLYM14194192).
- [42] J. Zhao, K. Dai, C. Liu, G. Zheng, B. Wang, C. Liu, J. Chen, C. Shen, A comparison between strain sensing behaviors of carbon black/polypropylene and carbon nanotubes/polypropylene electrically conductive composites, *Composites Part A: Applied Science and Manufacturing* 48 (2013) 129–136. doi:<https://doi.org/10.1016/J.COMPOSITESA.2013.01.004>.
- [43] S. Vidhate, J. Chung, V. Vaidyanathan, N. A. D’Souza, Resistive-conductive transitions in the time-dependent piezoresponse of pvdif-mwcnt nanocomposites, *Polymer Journal* 2010 42:7 42 (2010) 567–574. URL: <https://www.nature.com/articles/pj201044>. doi:<https://doi.org/10.1038/pj.2010.44>.
- [44] D. H. Griffiths, R. D. Barker, Two-dimensional resistivity imaging and modelling in areas of complex geology, *Journal of Applied Geophysics* 29 (1993) 211 – 226. doi:[https://doi.org/10.1016/0926-9851\(93\)90005-J](https://doi.org/10.1016/0926-9851(93)90005-J).
- [45] L. Yuan, S. Member, Y. Wei, J. Li, S. Member, Smart pressure e-mat for human sleeping posture and dynamic activity recognition, *arxiv* (2023). URL: <https://arxiv.org/abs/2305.11367v1>.
- [46] D. S. Tawil, D. Rye, M. Velonaki, Improved image reconstruction for an EIT-based sensitive skin with multiple internal electrodes, *IEEE Transactions on Robotics* 27 (2011) 425–435. doi:<https://doi.org/10.1109/TRO.2011.2125310>.
- [47] A. Yao, M. Soleimani, A pressure mapping imaging device based on electrical impedance tomography of conductive fabrics, *Sensor Review* 32 (2012) 310–317. doi:<https://doi.org/10.1108/02602281211257542>.

Appendix A. Noise Removal

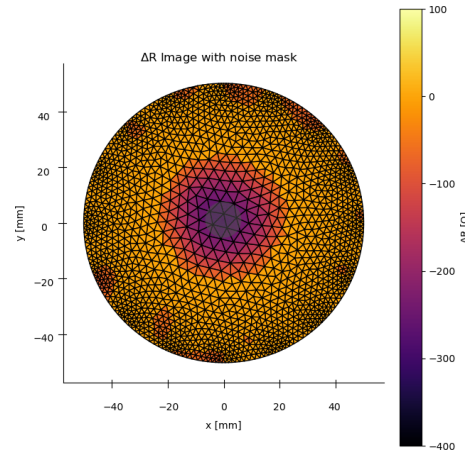


Figure A.16: Before executing the performance metrics calculations, the noise floor mask was applied to the 8% CBSR material shown in Figure 1

Appendix B. More Threshold Percentage Masks

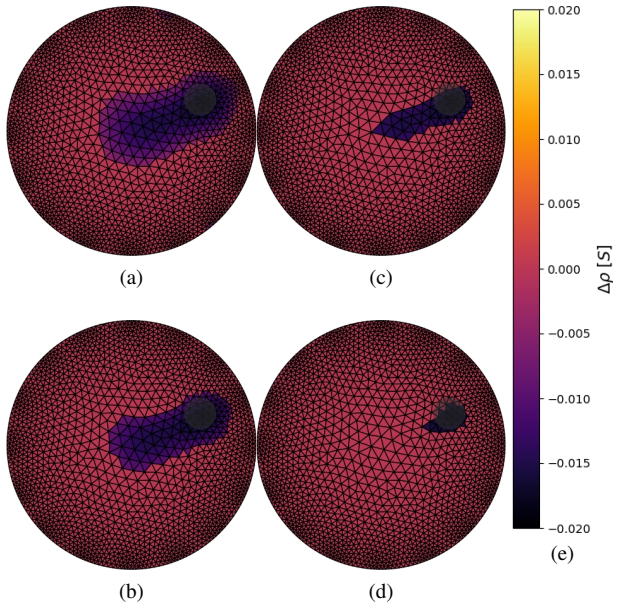


Figure B.17: A series of threshold percentage masks (a) 25%, (b) 50%, (c) 75%, and (d) 85% for the same reconstruction given in Figure A.15. (e) is the resistance change scale bar.

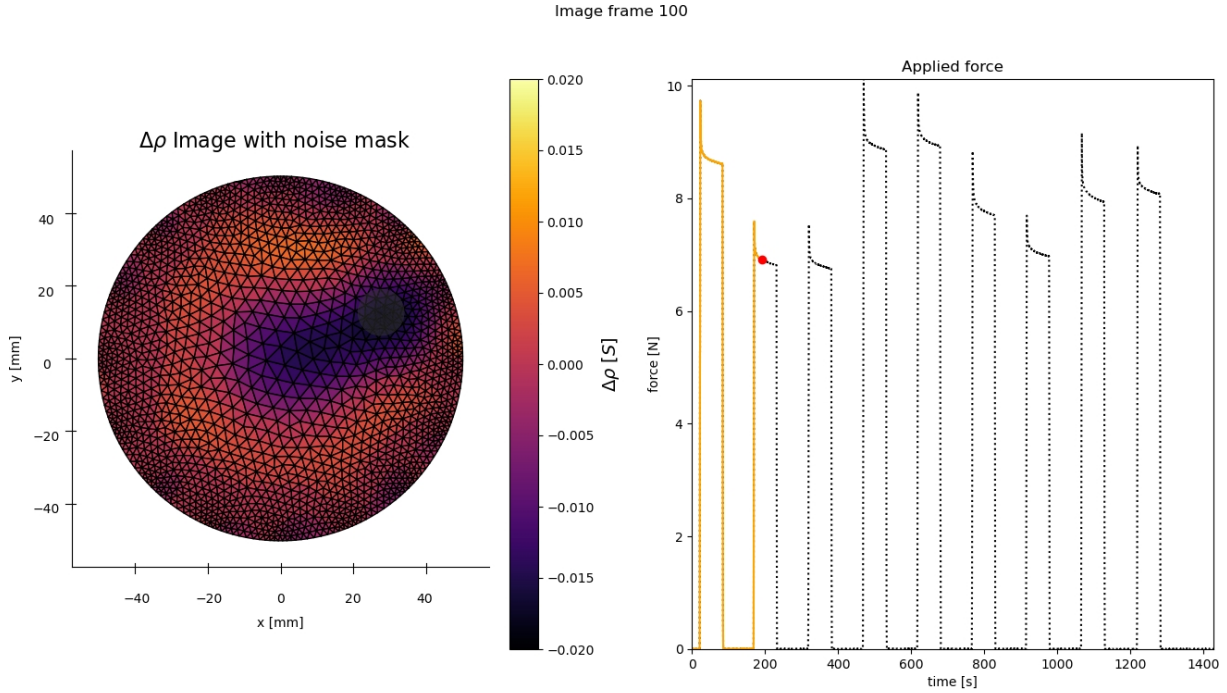


Figure A.15: An experimental snapshot. Left: Before executing the performance metrics calculations, the noise floor mask was applied to the 9% CBSR material. Right: Time series force data

Appendix C. Quasi-static Conductance Strain Fitted Data

Appendix D. 1D and 2D Strain Settling Times

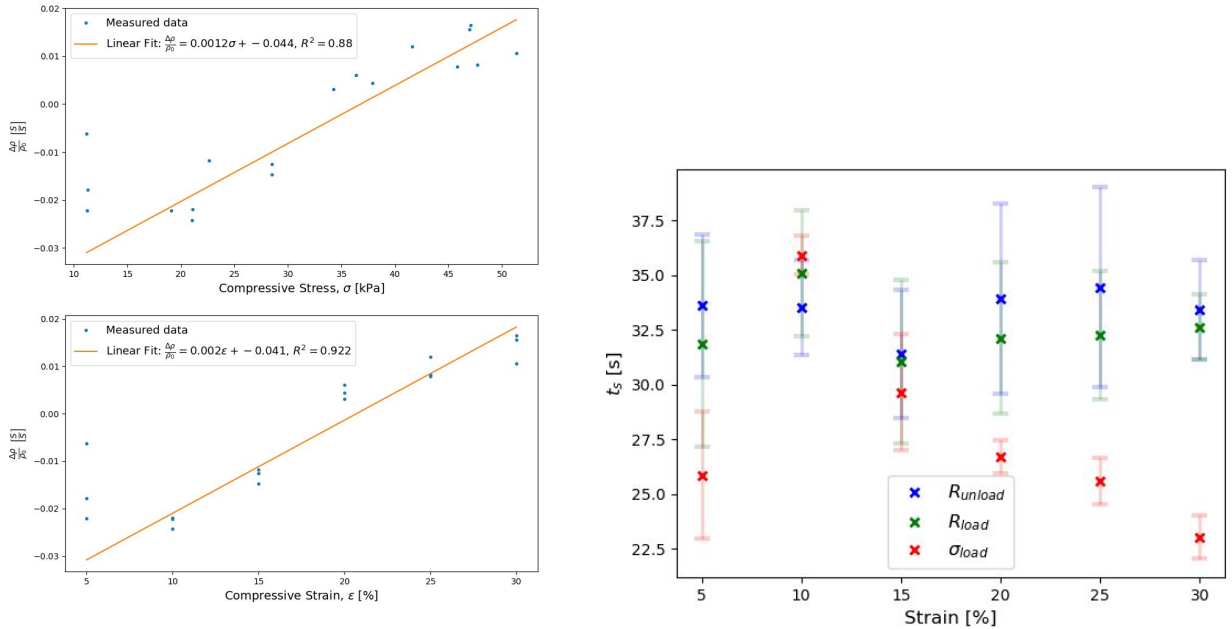


Figure C.18: Conductance change vs. stress (top) and strain (bottom) data and fitted curves for 9 wt% CBSR. The 5% strain values ignored as the std were larger than the conductance change values.

Figure D.19: Mean settling times for 5 - 30% compressive strain applied to CBSR 8 wt% with the error bars showing the standard deviation from 1D compressive test data.

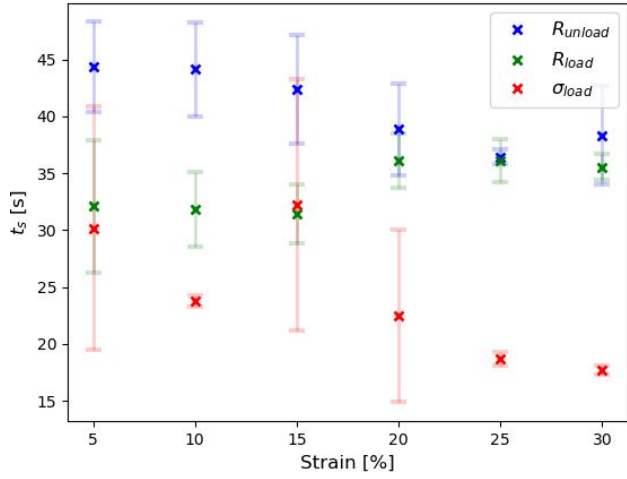


Figure D.20: Mean settling times for 5 - 30% compressive strain applied to CBSR 9 wt% with the error bars showing the standard deviation from 1D compressive test data.

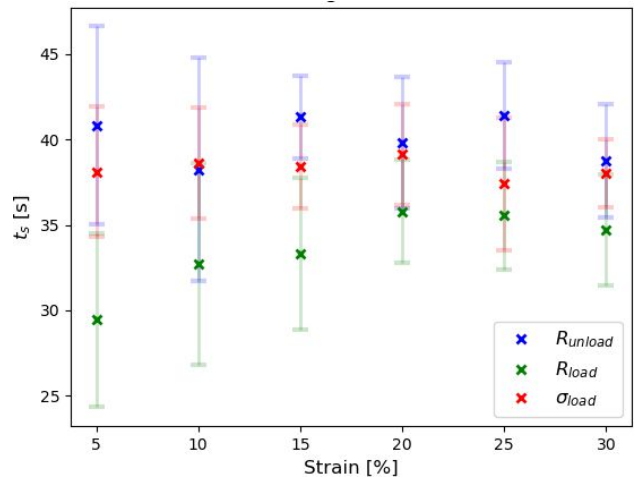


Figure D.22: Mean settling times for various strains applied to CBSR 9 wt% with the error bars showing the standard deviation of each settling time from the 2D EIT experimental data.

Appendix E. Performance Metrics Example

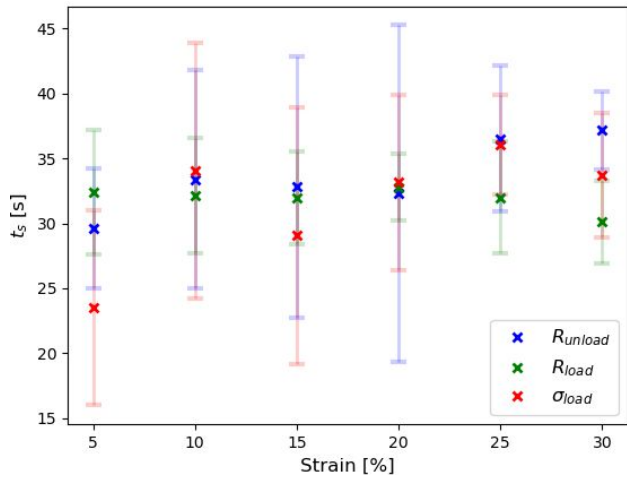


Figure D.21: Mean settling times for various strains applied to CBSR 8 wt% with the error bars showing the standard deviation of each settling time from the 2D EIT experimental data.

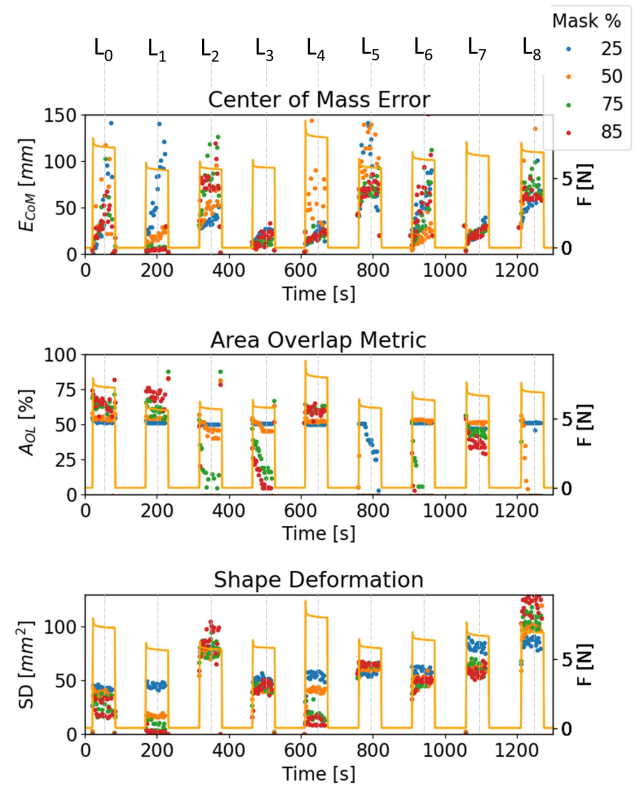


Figure E.23: Spatial performance metrics comparing threshold percentages of 25, 50, 75, and 85% for 9 wt% CBSR sample being loaded with 20% compressive strain in nine areas, L₀₋₈, shown in Fig 2.

Appendix F. Randomised test SD metrics data

Table F.6: CBSR 8 and 9 wt% mean and standard deviation for *SD* spatial performance metrics of ten random locations, L_{rand} and random strains ε

L_{rand} (r, θ) [mm, °]	ε [%]	8wt%SD [mm]	9wt%SD [mm]
(5.4, 10)	17.9	10.1 ± 0.8	9.8 ± 0.6
(29.8, 337)	24.0	62.2 ± 1.3	52.8 ± 1.3
(4.2, 317)	17.0	18.7 ± 5.9	21.7 ± 2.2
(34.0, 70)	10.9	20.2 ± 4.7	13.7 ± 0.8
(35.8, 137)	8.1	124.7 ± 2.8	81.5 ± 13.8
(9.6, 55)	13.8	24.8 ± 1.9	19.2 ± 1.8
(2.8, 260)	7.0	15.6 ± 4.5	12.7 ± 1.0
(11.2, 114)	10.0	4.5 ± 0.9	4.6 ± 0.6
(24.6, 241)	28.5	2.6 ± 0.1	2.6 ± 0.1
(16.6, 253)	23.6	0.3 ± 0.1	1.1 ± 0.1

Appendix G. Comparison of Non-EIT-based sensors

1st Author	Sensing principle	Sensing region material	Sensing region elastic modulus or shore hardness	Electrodes per sensing position	Repeatability	Time series data shown	Spatial resolution	Temporal resolution
Gilanizadehdizaj	Piezoresistive	Ecoflex30-00 rGO composite sponge	40 kPa	2 sensels / electrode	10 cycles for each stress	-	10 x 10 mm	-
Liang	Piezoresistive	Carbon black silicone composite	1.5 Mpa	0.625 sensels / electrode	50000 cycles	Yes.	12 x 12 mm	60 ms
Rossiter	Piezoresistive	Ecoflex graphene composite sponge	-	2 sensels / electrode	800 cycles	Yes.	10 x 10 mm	150 ms
Fu	Capacitive	PDMS, PET, Si, Sio2, Cu laminate	4000 Mpa	1 sensel / electrode	-	Real-time use of sensor demonstrated. Time-series data not explicitly given.	4 x 4 mm	-
Shimadera	Magnetic	Ecoflex 00-50	83 kPa	11 IC pins / sensel	30,000 cycles	Yes.	0.1 x 0.1 mm	15 ms
Ramuz	Optical	Polymer foam	-	2 sensels / electrode	-	-	10 x 10 mm	-
Yan	Optical	Super clear silicone	40 A	N/A. One fiber optic LASER and one camera.	Error increase of 1.7% over 30 days	Yes.	approx. 20 x 20 mm / 0 - 1100 um	Sample rate 1.6s. Training required.
Yang	Optical	PDMS	-	N/A. Two arrays of OLEDs and Organic Photo Detectors used.	900 cycles	Yes.	Not localised.	300 ms

Table G.7: All '-' values are not present in the paper reviewed

Appendix H. Comparison of EIT-based sensors

1st Author	DUT	Electrode type / number	Repeatability	Resistivity / Conductivity	Softness or max stretch range	Range of applied loads / strains	Transients compensated	Pre/post-processing algorithms for EIT image?	Spatial Performance metrics	Center-of-mass error value	Quant/qualitative pressure analysis
Ellingham (this work)	Custom carbon-black silicone composite	Gold plated electrical pin / x16	360 load events used for quantitative EIT experimental data	1.58 kΩ/cm - 14.2 kΩ/cm	Tested over 0 - 30%. Elastic moduli 98.1 kPa and 132.5 kPa	0 - 55.8 kPa	No. But transients are quantified.	Threshold eliminating negative values and a positive percentage thresholds	Center-of-mass error (E_{CoM}), Area overlap (A_{OL}) value, and shape deformation (SD) error value.	0.67 - 6.95 mm	Quant
Russo [31]	Polypyrrole coated nylon. EeonTex NW170-PI (Eonyx, Pinole, USA)	- / x16	Mean and variance calculated. No. of trials not mentioned.	102 S/cm to 103 S/cm cast film per ASTM F84 & D257	Max stretch = 40%. Tensile strength >450 N.	-	-	Threshold eliminating negative values and a positive percentage threshold	Size Error, Position Error (i.e. E_{CoM}) and Ringing (RNG)	1.4 - 6.7 %	Qual
Nagakubo [30]	PCR® piezoresistive silicone composite (JMT, Hidaka, Japan)	Crocodile clips / x16	x3 pulses of strain applied.	760 Ω/cm and 14.6 kΩ/cm	-	0 - 160 kPa	-	-	-	-	Quant
Hassan [20]	Copper sulfide nylon thread and Ag coated fabric	- / x16	-	-	-	0 - 150 kPa	-	-	-	-	Quant
Kato [21]	Pressure-sensitive conductive rubber	Copper tape / x16	-	-	-	-	-	-	-	-	Qual
Silvera-Tawil [46]	Piezoresistive stretchable fabrics (Eonyx, Pinole, USA) and (Less EMF, Inc., Latham, USA)	Circular chromium-plated brass eyelets of 7-mm diameter / x19	-	12.5 mS/sq and 660 mS/sq	-	-	-	50 and 75% thresholds	Resolution error (distinguishing between two touches) and distance error (i.e. E_{CoM})	~ 4 mm	Qual

Table H.8: All '-' values are not present in paper reviewed

1st Author	DUT	Electrode type / number	Repeatability	Resistivity / Conductivity	Softness or max stretch range	Range of applied loads / strains	Transients compensated	Pre/post-processing algorithms for EIT image?	Spatial Performance metrics	Center-of-mass error value range	Quant/ qualitative pressure analysis
Yoon [32]	Carbon-filled liquid silicone rubber, ELASTOSIL LR 3162 A/B (Wacker Ltd., Munich, Germany)	'Ribbon Crimp Ends used in jewelry craft' / x8 and x16	Mean and variance calculated. No. of trials not mentioned.	11 Ω·cm	54 A	5.5 - 15.8 kPa	Capacitive touch channel compensation	-	Distance error (i.e. E_{CoM})	3.8 - 18.4 mm	Quant
Sun [19]	Custom TPU-CB pressure-sensitive film	Silver conductive paste squares 10x10mm / x8	5500 load cycles	-	-	-	-	-	-	-	Qual
Yao [47]	Medical-grade silver-plated nylon Dorlastan fabric (Less EMF, Inc., Latham, USA)	Copper tape / x16	-	< 1 Ω/sq	Max stretch of 100% in length direction; 65% in width direction	-	'Relatively static condition, each image generated within 60 s'	-	-	-	Qual
Visentin [17]	Highly conductive medical-grade textile, MedTex180 (Shieldex®, Kleiner, Germany)	Crocodile clips / x8	'low repeatability rate, high hysteresis (especially for piezo-resistive sensors), and noise sensitivity'	< 1 Ω/sq	75- 155 % stretch	10.2 - 28.3 kPa	-	Centroid detection and threshold masking	-	-	Qual
Biasi [33]	Conductive ink, EptaTech (EptaNova, Luizago, Italy)	screen printed conductive ink / x16	6 positions x 5 trials	247.56 S/m (Estimated)	-	-	-	ANN used as well as EIT for solver. 40 % threshold.	-	-	Qual

Table H.9: All '-' values are not present in the paper reviewed